STRUCTURAL SCIENCE CRYSTAL ENGINEERING MATERIALS

ISSN 2052-5206

High-temperature Fe oxidation coupled with redistribution of framework cations in lobanovite, $K_2Na(Fe^{2+}{}_4Mg_2Na)Ti_2(Si_4O_{12})_2O_2(OH)_4$ – the first titanosilicate case

Elena S. Zhitova,[a]* Andrey A. Zolotarev,[a] Frank C. Hawthorne,[b] Sergey V. Krivovichev,[a,c] Viktor N. Yakovenchuk[c] and Alexey G. Goncharov[a]

[a]Institute of Earth Sciences, St Petersburg State University, University Emb. 7/9, St Petersburg, 199034, Russian Federation, [b]Department of Geological Sciences, University of Manitoba, 125 Dysart Road (Wallace Building), Winnipeg, MB R3T 2N2, Canada, and [c]Nanomaterials Research Center, Kola Science Center, Russian Academy of Sciences, Fersmana Str. 14, Apatity, 184209, Russian Federation. *Correspondence e-mail: zhitova_es@mail.ru

Received 19 February 2019
Accepted 30 April 2019

Edited by R. Černý, University of Geneva, Switzerland

Keywords: iron oxidation; dehydrogenation; cation redistribution/migration; astrophyllite-supergroup minerals; titanosilicate; heterophyllosilicate.

CCDC references: 1889997; 1889998; 1889999; 1890000; 1890001; 1890002; 1890003; 1890004; 1890005; 1890006; 1890007; 1890008; 1890009; 1890010; 1890011; 1890012; 1890013

Supporting information: this article has supporting information at journals.iucr.org/b

The high-temperature (HT) behaviour of lobanovite, $K_2Na(Fe^{2+}{}_4Mg_2Na)Ti_2(Si_4O_{12})_2O_2(OH)_4$, was studied using *in situ* powder X-ray diffraction in the temperature range 25–1000°C and *ex situ* single-crystal X-ray diffraction of 17 crystals quenched from different temperatures. HT iron oxidation associated with dehydroxylation starts at 450°C, similar to other ferrous-hydroxy-rich heterophyllosilicates such as astrophyllite and bafertisite. A prominent feature of lobanovite HT crystal chemistry is the redistribution of Fe and Mg+Mn cations over the *M*(2), *M*(3), *M*(4) sites of the octahedral (**O**) layer that accompanies iron oxidation and dehydroxylation. This HT redistribution of cations has not been observed in titanosilicates until now, and seems to be triggered by the need to maintain bond strengths at the apical oxygen atom of the TiO_5 pyramid in the heteropolyhedral (**H**) layer during oxidation–dehydroxylation. Comparison of the HT behaviour of lobanovite with five-coordinated Ti and astrophyllite with six-coordinated Ti shows that the geometry of the Ti polyhedron plays a key role in the HT behaviour of heterophyllosilicates. The thermal expansion, geometrical changes and redistribution of site occupancies which occur in lobanovite under increasing temperature are reported. A brief discussion is given of minerals in which the cation ordering (usually for Fe and Mg) occurs together with iron oxidation–dehydroxylation at elevated temperatures: micas, amphiboles and tourmalines. Now this list is expanded by the inclusion of titanosilicate minerals.

1. Introduction

Lobanovite, $K_2Na(Fe^{2+}{}_4Mg_2Na)Ti_2(Si_4O_{12})_2O_2(OH)_4$, is a member of the devitoite group which is a part of the astrophyllite supergroup (Sokolova *et al.*, 2017*a*) and belongs to the family of heterophyllosilicates which bear structural resemblances to different sheet silicate minerals (Ferraris, 2005, 2008). The crystal structures of both (i) heterophyllosilicates and (ii) phyllosilicates (sheet silicates, *e.g.* clays and micas) contain octahedral layers that are sandwiched between (i) heteropolyhedral (tetrahedra–octahedra/pyramid) layers or (ii) solely tetrahedral layers. Lobanovite is chemically and structurally similar to astrophyllite, which explains the rather convoluted history of its description and approval by the international mineralogical community (Sokolova *et al.*, 2017*b*).

The general structural motif of lobanovite (Fig. 1) consists of heteropolyhedral (**H**) and octahedral (**O**) layers stacked

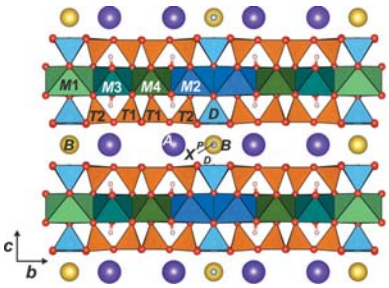

along [001] in the **HOH** periodicity. The **O** layer consists of edge-sharing $M(1)$–$M(4)$ octahedra occupied by Fe, Mg, Na and minor Mn. The **H** layer consists of corner-sharing T_4O_{12} (T = Si, Al) ribbons running along [100] and connected along [010] by DO_5 pyramids (D = Ti with minor Nb and traces of Zr). In lobanovite, adjacent **HOH** blocks are connected through interlayer alkali and alkaline earth cations: K, Na, Ca, Sr and Ba (Peng & Ma, 1963; Shi *et al.*, 1998; Sokolova & Cámara, 2008). The general formula of astrophyllite-supergroup minerals is $A_{2p}B_rC_7D_2(T_4O_{12})_2X^{O}{}_{D2}X^{O}{}_{A4}X^{P}{}_{Dn}$, where C and D are cations of the **O** and **H** sheets, C = $^{[6]}$(Fe^{2+}, Mn, Fe^{3+}, Na, Mg or Zn) at the M(1–4) sites; D = $^{[6,5]}$(Ti, Nb, Zr, Fe^{3+}); T = Si, minor Al; $A_{2p}B_r$ is the composition of the intermediate block where p = 1, 2; r = 1, 2; A = K, Cs, Li, Ba, H_2O, □; B = Na, Ca, Ba, H_2O, □; $X = X^{O}{}_{D2}X^{O}{}_{A4}X^{P}{}_{Dn}$ = O, OH, F and H_2O; n = 0, 1, 2 (Sokolova *et al.*, 2017*a*).

Heterophyllosilicates have not yet found a technological application, though the general structural motif of heterophyllosilicates (**HOH**) is structurally related to that of clays (**TOT**) which are widely considered as functional materials (Murray, 1991; Mukherjee, 2013). There are plenty of crystal-chemical data on heterophyllosilicates at room temperature (see *e.g.* Piilonen, Lalonde *et al.*, 2003; Piilonen, McDonald *et al.*, 2003; Sokolova, 2006; Ferraris *et al.*, 2008; Cámara *et al.*, 2010; Stepanov *et al.*, 2012; Agakhanov *et al.*, 2016; Sokolova & Hawthorne, 2016; Jin *et al.*, 2018; Sokolova *et al.*, 2018), but the same cannot be said of their behaviour at non-ambient conditions.

Recent laboratory studies of potential transformation of heterophyllosilicates have revealed novel features of these compounds. Study of the ion-exchange properties of three structurally related heterophyllosilicates, murmanite, lomonosovite and vigrishinite (Lykova, Chukanov, Tarasov *et al.*, 2013; Lykova, Chukanov, Kazakov *et al.*, 2013; Lykova *et al.*, 2015*a*,*b*), indicated their high affinity and selectivity for uptake of chalcophile elements, and, more surprisingly, that cation exchange may occur for both intermediate-block cations and cations of **O** and **H** layers.

Our recent studies on the high-temperature behaviour of some heterophyllosilicates have shown that Fe^{2+}-(OH)-rich members undergo iron oxidation together with dehydroxylation that may also be coupled with defluorination: astrophyllite (Zhitova, Krivovichev *et al.*, 2017), bafertisite (Zhitova, Zolotarev *et al.*, 2017) and Fe^{2+}-poor barytolamprophyllite (Zhitova *et al.*, 2018). These newly discovered crystal-chemical aspects of layered titanosilicates point to a more complicated crystal chemistry, insights of which can be obtained by examining these compounds at non-ambient conditions.

Here we describe the high-temperature behaviour of lobanovite which, in addition to iron oxidation–dehydroxylation, undergoes cation rearrangement in the **O** layers (without defluorination), extending our knowledge on possible structural adjustment of minerals to temperature (or other external factors) via optimization of bond valences by local ordering of atoms. New data on lobanovite will be compared with the earlier data on astrophyllite (Zhitova, Krivovichev *et al.*, 2017), and hence we provide a brief crystal-chemical comparison of these two minerals. The main chemical difference between lobanovite and astrophyllite is the presence of M^+ cations [Na occupies the M(1) site] in the **O** layer of lobanovite, whereas in astrophyllite only M^{2+} and minor M^{3+} cations occur in the **O** layer [M(1)–M(4) sites]. The presence of monovalent cations in the **O** layers of lobanovite causes a different distribution of bond valences incident upon the oxygen atoms and results in a different (compared with astrophyllite) position of the **H** layers relative to the **O** layers (Fig. 1) which leads to different symmetries of these two minerals: lobanovite is monoclinic, whereas astrophyllite is triclinic [see details in Sokolova & Cámara (2008)]. Another principal crystal-chemical difference between astrophyllite and lobanovite is in the geometry of the D polyhedra: in astrophyllite, the D site is six-coordinated (as in most of the heterophyllosilicates), whereas in lobanovite the D site is five-coordinated ~80% and six-coordinated ~20% as reflected in the occupancy of the $X^{P}{}_{D}$ site (Fig. 1), ~20% by F. This is

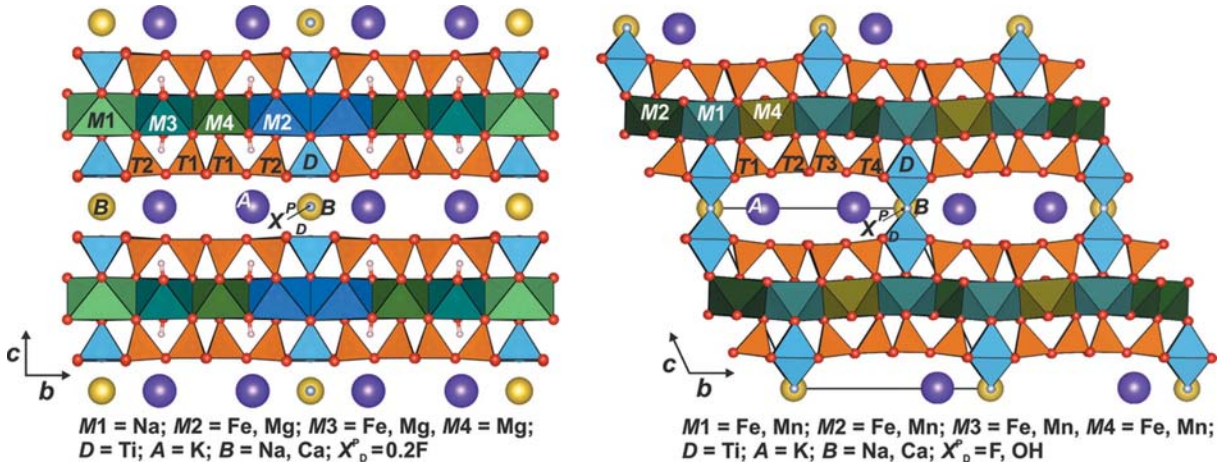

Figure 1
Two **HOH** blocks of the crystal structure of lobanovite (left) and astrophyllite (right).

because the sample studied by Sokolova & Cámara (2008) was a solid solution between a $^{B}Na\square^{P}{}_{D}$ and a $^{B}CaF^{P}{}_{D}$ end-member. The *D* site is fivefold coordinated in the present study because it is coordinated by F only for 20% (sixfold coordination), for the remaining 80% the F site is vacant (fivefold coordination).

2. Materials

The lobanovite studied in this work originates from Mt Niorkpakhk, Khibiny, Kola peninsula, Russia (Yakovenchuk *et al.*, 2005). The initial, unheated sample is labelled Lb25. The temperature-induced transformation of lobanovite (described in detail below) is irreversible, and the high-temperature modifications are stable at room temperature, allowing *ex situ* study. Samples were annealed in an oven using the following procedure [as for astrophyllite (Zhitova, Krivovichev *et al.*, 2017)]: heating from room temperature to *T* (°C) over 30 min and constant heating at this *T* for 1 h, followed by cooling (< 30 min); the resultant material was used for the *ex situ* studies. The annealed phases are denoted Lb*T*, *e.g.* Lb300 means that the sample was annealed at 300°C following the procedure described above. The notation Lb630-2 means that a second sample was annealed independently (from Lb630-1 and Lb630-3) in order to check for consistency. The work involved 17 crystals (including untreated lobanovite): Lb25, Lb300, Lb450, Lb500, Lb550, Lb570-1, Lb570-2, Lb590-1, Lb590-2, Lb590-3, Lb610, Lb630-1, Lb630-2, Lb650, Lb670, Lb690 and Lb710.

3. Experimental

3.1. Chemical composition

Sample Lb25 was mounted on an epoxy block and polished. The chemical composition of the sample was determined with a scanning electron microscope S3400N equipped with an AZtec analyzer (Energy 350) operating in EDS mode at 20 kV, 1.5 nA and with a 5 µm spot size. The standards used were NaCl (Na), KCl (K), $CaSO_4$ (Ca), BaF_2 (Ba), SrF_2 (Sr), FeS_2 (Fe), MgO (Mg), Mn (Mn), SiO_2 (Si), Al_2O_3 (Al), Ti (Ti), Nb (Nb), Zr (Zr), BaF_2 (F).

Mean analytical results are given in Table 1 together with previously published chemical data on lobanovite. The crystals of lobanovite are chemically homogeneous. Our data are in good agreement with the previously published chemical compositions of the mineral (Table 1). The chemical formula of lobanovite calculated on the basis of Σ⟨anions⟩ = 30.2 is $(K_{1.95}Ba_{0.03})_{\Sigma 1.98}(Na_{0.77}Ca_{0.19}Sr_{0.01})_{\Sigma 0.97}(Fe^{2+}{}_{3.24}Mg_{2.30}Na_{1.02}Mn_{0.45})_{\Sigma 7.00}(Ti_{1.93}Nb_{0.12})_{\Sigma 2.05}[(Si_{7.88}Al_{0.06})_{\Sigma 7.95}O_{24}]O_2(OH)_{4.00}F_{0.16}$. The basis for the chemical formula calculations (30.2 anions) assumes full occupancy of all oxygen sites and occupancy of the $X^{P}{}_{D}$ site ~20% by F as indicated by both our structure refinements and previously published data (Sokolova & Cámara, 2008).

Table 1
Chemical composition of lobanovite.

NA – not analysed, ND – not determined.

					The holotype locality		
Present work					X-ray Laboratory, Hubei Geologic College (1974)		Sokolova & Cámara (2008)
Constituent	wt%	wt% ranges	Constituent	a.p.f.u.†	Constituent	wt%	wt%
K_2O	7.60	7.50–7.70	K	1.95	K_2O	7.28	7.66
BaO	0.41	0.21–0.67	Ba	0.03	BaO	NA	0.13
			Σ*A*	1.98			
Na_2O‡	4.62	4.43–4.79	Na	0.77	Na_2O	5.38	4.22
CaO	0.86	0.74–1.01	Ca	0.19	CaO	1.15	0.65
SrO	0.09	0.04–0.19	Sr	0.01	SrO	NA/ND	NA/ND
			Σ*B*	0.97			
FeO§	19.35	19.09–20.33	Fe^{2+}	3.24	FeO	17.91	18.86
MgO	7.71	6.65–7.94	Mg	2.30	MgO	6.39	6.72
MnO	2.62	2.31–2.82	Mn	0.45	MnO	4.00	4.21
			Na	1.02	Fe_2O_3	2.95	ND
			Σ*C*	7.00			
TiO_2	12.78	11.83–13.65	Ti	1.93	TiO_2	12.18	13.11
Nb_2O_5	1.27	0.36–2.11	Nb	0.12	Nb_2O_5	NA	0.64
ZrO_2	0.04	0.00–0.14	Zr	0.00	ZrO_2	NA/ND	NA/ND
			Σ*D*	2.05			
SiO_2	39.19	38.57–39.97	Si	7.88	SiO_2	37.98	39.72
Al_2O_3	0.26	0.11–0.40	Al	0.06	Al_2O_3	1.11	0.24
			Σ*T*	7.95			
F	0.25	0.21–0.29	F	0.16	F	0.45	0.29
H_2O	3.00¶		H_2O	4.00	H_2O	3.44	3.00¶
F=O_2	−0.11				F=O_2	−0.19	−0.12
Total	99.93				Total	100.03	99.33

† A.p.f.u. calculated on the basis of Σ anions = 30.2. ‡ The total Na_2O is given although Na occurs in two crystallographic sites *B* and *C* and is divided between them based on structural data (see a.p.f.u. column). § By Mössbauer spectroscopy. ¶ Calculated from structure refinement.

3.2. Thermal analysis

Differential scanning calorimetry (DSC) and thermogravimetric analysis (TG) were done for Lb25 using a DSC/TG Netzsch STA 449F3 instrument in the 30–1000°C temperature range at a ramp rate of 10°C min^{-1}, gas flow 20 ml min^{-1} by heating the samples under Ar–O atmosphere. An exothermic effect was detected at 644.2°C during heating in air (Fig. 2), associated with a mass loss of ~0.4% corresponding to the

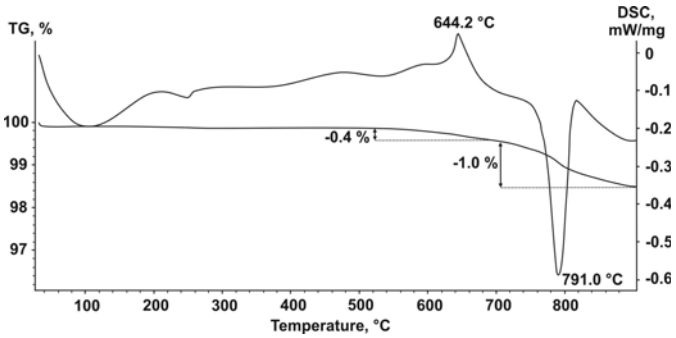

Figure 2
DTA and TG curves of lobanovite.

release of hydrogen. The second mass loss of ∼1% is associated with mineral decomposition and occurs at 791°C.

3.3. Mössbauer and IR spectroscopy

Mössbauer spectra were collected at room temperature (RT) using a ^{57}Co(Rh) source for the samples Lb25, Lb300, Lb450, Lb550 and Lb670. The spectrometer was calibrated using the spectrum of metallic iron at RT. Powdered absorbers containing ∼5 mg Fe per cm^2 were pressed in plastic discs and fixed on a special aluminium holder to avoid preferred orientation of mineral grains. The spectra were approximated by a sum of Lorentzian lines using the *MOSSFIT* software. The relative amounts of Fe^{2+} and Fe^{3+} and their site positions in the crystal lattice were determined from integral doublet intensities and hyperfine parameters, assuming equal Mössbauer effect probabilities for Fe^{2+} and Fe^{3+} at different sites.

The Mössbauer spectrum of lobanovite (Fig. 3) is completely different from those of other astrophyllite-group minerals: they show a single quadrupole-split doublet (Cámara *et al.*, 2010; Zhitova, Krivovichev *et al.*, 2017), whereas the Mössbauer spectrum of lobanovite (Lb25) shows two quadrupole-split doublets of equal intensity. Presumably this radical difference in the spectra is caused by the presence of Na completely occupying the *M*(1) octahedron.

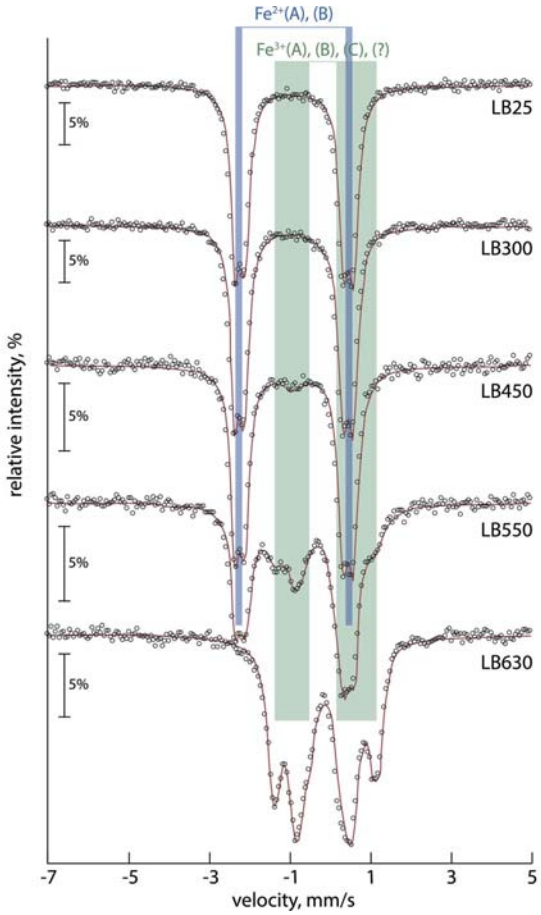

Figure 3
The evolution of Mössbauer spectra of lobanovite with temperature.

IR spectra of lobanovite (Lb25) and its high-temperature (HT) modification (Lb670) were recorded using a Bruker Vertex IR spectrometer. The measurements were done at RT using a KBr pellet technique. Fig. 4 shows the IR spectra of lobanovite (Lb25) and its HT modification (Lb670): the IR spectrum of the fresh material (Lb25) contains a broad band at 3600–3000 cm^{-1}, which is absent in the spectrum of Lb670, indicating that deprotonation has taken place.

3.4. *In situ* high-temperature powder X-ray diffraction

In situ high-temperature powder X-ray diffraction (HTXRD) experiments on lobanovite (Lb25) up to 1000°C (Fig. 5) were done in air using a Rigaku Ultima IV powder X-ray diffractometer (Cu $K\alpha_{1+2}$ radiation, 40 kV, 30 mA, Bragg–Brentano geometry, position-sensitive detector D-Tex Ultra) with a Rigaku HT 1500 high-temperature attachment. A thin powder sample was deposited on a Pt sample holder (20 × 12 × 2 mm) from a heptane suspension. Silicon was used as an internal standard. The temperature step and the heating rate were 25°C and 4° min^{-1}, respectively, and the collecting time at each temperature step was about 30 min. The reversibility of the observed phase transformation was checked by re-recording the powder patterns for sample Lb25 heated to 650°C and then cooled to RT.

The unit-cell parameters (Table S1) were refined by the Rietveld method using *Topas* 4.2 (Bruker, 2009), with the monoclinic structure model, space group *C*2/*m*, with the starting unit-cell parameters a = 5.3327 (2), b = 23.1535 (9), c = 10.3775 (4) Å, β = 99.615 (1)°, V = 1263.3 (1) Å^3 (Sokolova &

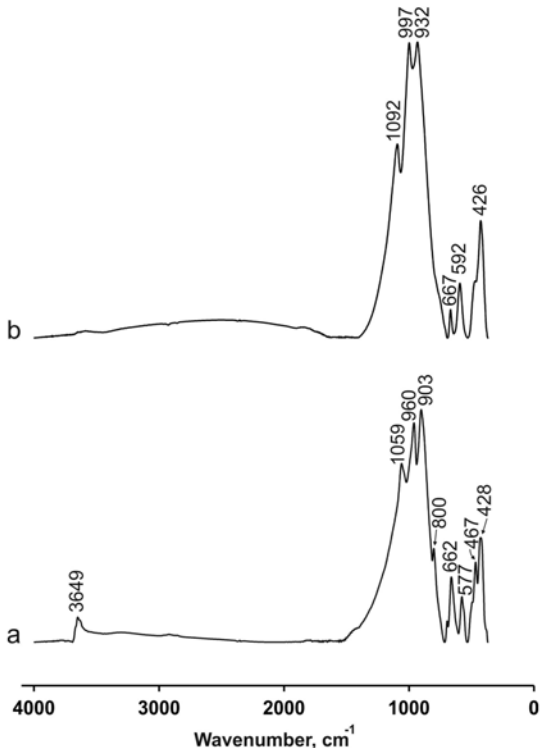

Figure 4
IR spectra of lobanovite (Lb25) and its HT modification (Lb670).

Cámara, 2008). The refinement was based on the reflections in the 2θ region 10–60°. Rietveld refinement was done with the fixed atom coordinates, site scattering and isotropic displacement parameters. The refinement of the unit-cell parameters was done in the temperature ranges 25–500°C and 600–750°C for lobanovite and its HT modification, respectively (Fig. 6). Broadening of some reflections for the patterns recorded at 525, 550 and 575°C indicates the coexistence of lobanovite and its HT modification. Therefore, the unit-cell parameters in the 525–575°C temperature range could not be determined reliably. Neutral scattering factors were used for all atoms. The background was modelled using a Chebyshev polynomial approximation of the 12th order. The peak profile was described using the fundamental parameters approach. Refinement of preferred orientation parameters confirmed the presence of significant preferred orientation along the [001] direction.

The main coefficients of the thermal expansion tensor were determined using a second-order approximation of temperature dependencies for the unit-cell parameters (Fig. 6) in the range 25–525°C for lobanovite and 575–750°C for its HT modification, using the *DTC* program (Belousov & Filatov, 2007; Bubnova *et al.*, 2013); thermal expansion coefficients are given in Table S2. The figures displaying thermal expansion coefficients were drawn using the *TEV* program (Langreiter & Kahlenberg, 2015) and are shown in Fig. 7.

It can be seen in Fig. 5 that there is an abrupt shift of reflections to higher angles (in 2θ) at ~550°C, which manifests in the formation of the HT modification of lobanovite. Mineral decomposition occurs at $T \geq 800$°C. The variation in the unit-cell parameters as a function of T is shown in Fig. 6, where two separate dependencies can be seen for lobanovite (25–525°C)

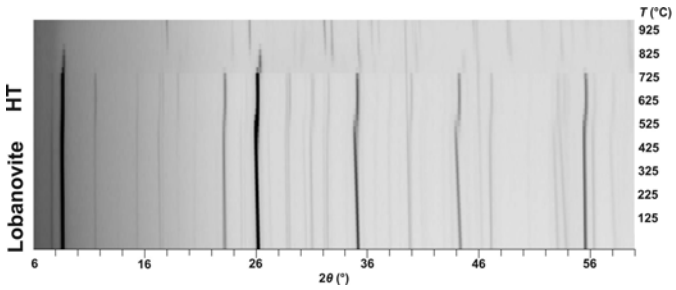

Figure 5
Powder diffraction patterns recorded for lobanovite in the temperature range 25–1000°C.

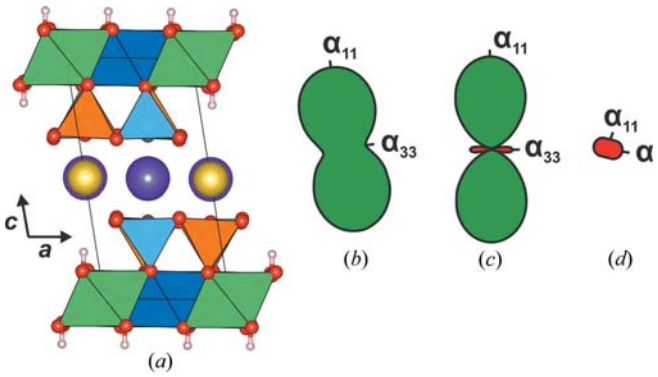

Figure 7
The crystal structure of lobanovite (*a*) and figures of thermal expansion/contraction coefficients at T = 200°C (*b*), 400°C (*c*) and 650°C (*d*).

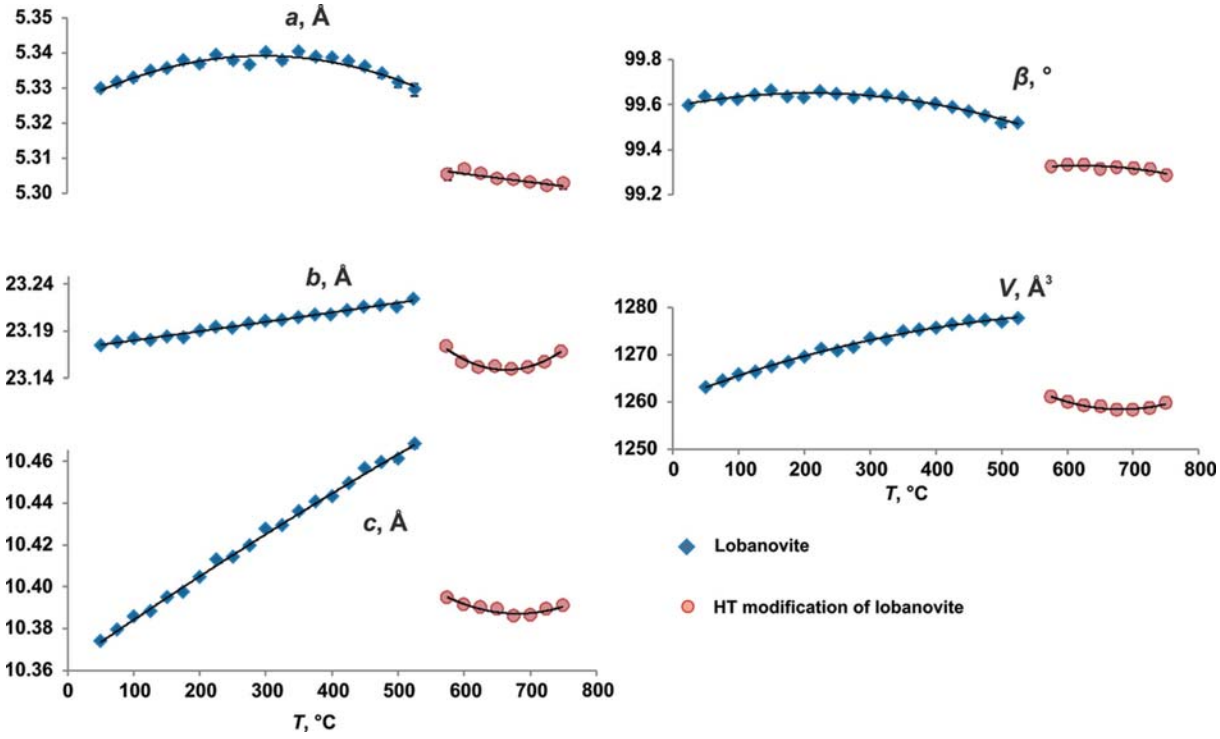

Figure 6
The refined unit-cell parameters for lobanovite and its HT modification. Standard uncertainties fall within the limits of the symbols.

Table 2
Crystal-chemical features of lobanovite and its HT modification.

Crystallographic data	Lobanovite (Lb25)	HT modification (Lb710)
Simplified chemical formula	$K_2Na(Fe^{2+}{}_4Mg_2Na)Ti_2(Si_4O_{12})_2O_2(OH)_4$	$K_2Na(Fe^{3+}{}_4Mg_2Na)Ti_2(Si_4O_{12})_2O_2O_4$
Symmetry	Monoclinic	Monoclinic
Space group	*C*2/*m*	*C*2/*m*
a, *b*, *c* (Å)	5.3499 (3), 23.268 (1), 10.4149 (4)	5.3110 (3), 23.141 (1), 10.2979 (6)
β (°)	99.658 (4)	99.476 (5)
V (Å^3)	1278.1 (1)	1248.4 (1)

Occupancies of cation sites

	Lobanovite (Lb25)			HT modification (Lb710)		
		Site scattering			Site scattering	
Site	Site population†	Reference	Calculated†	Site population	Reference	Calculated†
M(1)	$Na_{1.0}$	10.91 (1)	11.0	$Na_{1.0}$	9.6 (1)	11.0
M(2)	$Fe^{2+}{}_{1.62}Mg_{0.21}Mn_{0.17}$	48.8 (2)	48.9	$Fe^{3+}{}_{0.80}Mg_{0.75}Mn_{0.45}$	38.3 (2)	41.0
M(3)	$Fe^{2+}{}_{0.97}Mg_{0.89}Mn_{0.14}$	39.5 (2)	39.5	$Fe^{3+}{}_{1.48}Mg_{0.52}$	41.9 (2)	44.7
M(4)	$Mg_{1.32}Fe^{2+}{}_{0.54}Mn_{0.14}$	33.5 (2)	33.5	$Fe^{3+}{}_{1.04}Mg_{0.96}$	35.0 (2)	37.4
D	$Ti_{1.9}Nb_{0.1}$	43.2 (1)	45.9	$Ti_{1.9}Nb_{0.1}$	44.0 (1)	45.9
T(1)	$Si_{1.00}$	13.58 (6)	14.0	$Si_{1.00}$	13.51 (6)	14.0
T(2)	$Si_{1.00}$	13.51 (6)	14.0	$Si_{1.00}$	13.40 (7)	14.0
A	$K_{1.96}\square_{0.04}$	36.9 (2)	37.2	$K_{1.96}\square_{0.04}$	37.1 (2)	37.2
ΣB	$Na_{0.80}Ca_{0.20}$	11.9 (4)	12.8	$Na_{0.80}Ca_{0.20}$	12.3 (5)	12.8
$X^P{}_D$	$\square_{0.83}F_{0.17}$	1.53 (8)	1.53	$\square_{0.83}F_{0.17}$	1.1 (1)	1.53

Geometrical parameters. Superscripted number in brackets indicates the coordination number, NC indicates not calculated, DI indicates distortion index and BAV indicates bond-angle variance.

	Lobanovite (Lb25)				HT modification (Lb710)			
	Average bond length (Å)	Calculated bond length (Å)†	DI‡	BAV§	Average bond length (Å)	Calculated bond length (Å)†	DI‡	BAV§
M(1)$^{[6]}$	2.384	2.42	0.025	85.8	2.390	2.42	0.031	103.7
M(2)$^{[6]}$	2.172	2.12	0.026	69.3	2.139	2.14	0.042	97.5
M(3)$^{[6]}$	2.120	2.10	0.024	37.3	2.070	2.08	0.047	46.4
M(4)$^{[6]}$	2.102	2.08	0.008	39.0	2.088	2.10	0.044	74.5
D$^{[5]}$	1.914	1.89	0.036	NC	1.911	1.89	0.027	NC
T(1)$^{[4]}$	1.631	1.66	0.008	5.4	1.626	1.66	0.006	5.1
T(2)$^{[4]}$	1.632	1.66	0.010	14.2	1.625	1.66	0.009	9.7
A$^{[13]}$	3.193	3.04	0.061	NC	3.152	3.04	0.055	NC
B$^{[10]}$	2.570	2.42	0.022	NC	2.531	2.42	0.023	NC

† See calculations in Section 4.3. † Calculated bond lengths from assigned site occupancies using ionic radii by Shannon (1976). ‡ Distortion index (DI) was calculated using the *Vesta* program as $D = (1/n)\sum_{i=1}^{n}(|l_i - l_{av}|/l_{av})$, where l_i = the distance between the central atom and the *i*th coordinating atom, l_{av} = the average bond length (Momma & Izumi, 2011). § Bond-angle variance (BAV) [originally described as octahedral angle variance or tetrahedral angle variance by Robinson *et al.* (1971)] was calculated using the *Vesta* program (Momma & Izumi, 2011) as $\sigma^2 = [1/(m-1)]\sum_{i=1}^{m}(\varphi_i - \varphi_0)^2$, where *m* is the number of faces in the polyhedron × 3/2 (*i.e.* number of bond angles), φ_i is the *i*th bond angle and φ_0 is the ideal bond angle for a regular polyhedron.

and its HT modification (575–775°C). The eigenvalues of the thermal expansion/contraction coefficients along the crystallographic axes and the orientation of the principal axes of the thermal expansion tensor are given in Table S2.

3.5. *Ex situ* single-crystal X-ray diffraction of lobanovite and its HT modification

Seventeen crystals of lobanovite (Lb25, Lb300, Lb450, Lb500, Lb550, Lb570-1, Lb570-2, Lb590-1, Lb590-2, Lb590-3, Lb610, Lb630-1, Lb630-2, Lb650, Lb670, Lb690 and Lb710) were examined in air at RT using a Bruker SMART APEX single-crystal diffractometer operated at 50 kV, 40 mA, and equipped with a CCD area detector and graphite-monochromated Mo *K*α radiation (Mo *K*α, $\lambda = 0.71073$ Å). The data were collected and processed using the Bruker software *APEX2* (Bruker, 2014). The intensity data were reduced and corrected for Lorentz, polarization and background effects using the Bruker software *APEX2*. A semi-empirical absorption correction based upon the intensities of equivalent reflections was applied (*SADABS*: Sheldrick, 2015).

The diffraction data obtained during single-crystal X-ray experiments were indexed in a monoclinic unit cell, space group *C*2/*m* (Table 2). Crystal structures were refined using the atom coordinates from Sokolova & Cámara (2008) with the *SHELXL* program package (Sheldrick, 2015). Site occupancies were refined for all cation sites and the *F* ($X^P{}_D$) anion site for all 17 modifications using the following scattering curves: *M*(1) (Na), *M*(2) (Fe), *M*(3) (Fe), *M*(4) (Mg), *D* (Ti), *T*(1) (Si), *T*(2) (Si), *A* (K), *B* (Na) and *F* (F) (site notations – italic). The atom coordinates, isotropic displacement parameters and refined site scattering data are given in the elec-

tronically deposited cifs, CCDC 1889997–1890013. The comparative crystal-chemical data for lobanovite (Lb25) and its HT modification (Lb710) are given in Table 2: site populations for cation sites, average and calculated bond distances, distortion indexes and bond-angle variance.

4. Results

4.1. Thermally induced iron oxidation–dehydroxylation: geometrical changes

Lobanovite undergoes HT iron oxidation associated with dehydroxylation (deprotonation) via the reaction $Fe^{2+} + OH^- \rightarrow Fe^{3+} + O^{2-} + \frac{1}{2}H_2 \uparrow$, at $T > 450$°C, accompanied by its transformation to the HT phase with the same symmetry but contracted unit-cell parameters. The transformation is similar to those observed for astrophyllite (Zhitova, Krivovichev *et al.*, 2017) and bafertisite (Zhitova, Zolotarev *et al.*, 2017). Comparison of unit-cell parameters of lobanovite and its HT modification (Fig. 6) shows that the main contraction occurs along the layer-stacking direction, *i.e.* [001]. The main contraction refers to the distance between two adjacent **HOH** blocks, *i.e.* to collapse of the intermediate block from 3.53 Å (Lb25) to 3.42 Å (Lb710), which is possibly the result of a redistribution of bond strengths in the HT modification in comparison with lobanovite. This is also reflected by contraction of A–φ and B–φ interatomic distances (Table 2).

Here we discuss the geometrical changes of polyhedra in the **O** and **H** layers (excluding intermediate-block A and B sites) caused by iron oxidation and dehydroxylation using mean bond lengths and distortion indices (see comparison of Lb25 and Lb710 in Table 2). These parameters are approximately constant for the $M(1)$ octahedron and the $T(1)$ and $T(2)$ tetrahedra, although there is a slight elongation of the apical $T(1)$–O(6) and $T(2)$–O(2) bonds (Fig. 8) and contraction of the $T(1)$–basal oxygen atom and $T(2)$–basal oxygen atom distances. The distortion indices of the $M(2)$, $M(3)$, $M(4)$ octahedra increase with increasing temperature from ~0.025 to ~0.045 for $M(2)$ and $M(3)$, and from 0.008 to 0.044 for $M(4)$ (Table 2). The mean bond lengths (and volumes) of the $M(2)$, $M(3)$, $M(4)$ octahedra decrease with the increase in annealing temperature, consistent with the change of iron oxidation state from ferrous to ferric. There is an increase observed for the $\langle D$–O(1)$\rangle$ apical bonds from 1.735 (Lb25) to 1.779 (Lb710) Å.

In the **O** layer, the bond lengths of the $M(2)$, $M(3)$ and $M(4)$ octahedra decrease and their distortion increases, both resulting in the flattening of the **O** layer from 2.26 (Lb25) to 2.23 (Lb710) Å. The distortions of the D pyramid and $T(1)$, $T(2)$ tetrahedra of the **H** layer do not change significantly, but there is an observable increase in the $D/T(1)/T(2)$–apical oxygen bonds (Fig. 8).

4.2. Thermal iron oxidation–dehydroxylation: redistribution of site occupancies by single-crystal X-ray diffraction data

The variation in site scattering values with the annealing temperature for lobanovite and its HT modifications is summarized in Fig. 9 (exact values are given in Table 2 for Lb25 and Lb710), from which we can clearly see that the refined site scattering values remain nearly constant for the $M(1)$, D, $T(1)$, $T(2)$, A and B sites (Fig. 9). In contrast, for the $M(2)$ site, the site scattering begins to decrease at $T \geq 450$°C and then drops dramatically at 550–590°C, when Fe is completely oxidized. The opposite situation is observed for the $M(3)$ and $M(4)$ sites, where the site scattering increases (Fig. 9).

Combining our knowledge of the site occupancies in untreated lobanovite and the changes in the site occupancies observed here, it may be concluded that iron oxidation and dehydroxylation are accompanied by the migration of Fe from the $M(2)$ site to the $M(3)$ and $M(4)$ sites. The opposite

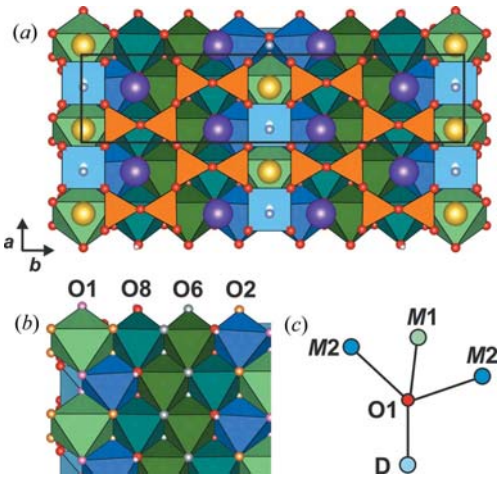

Figure 8
(*a*) (110) projection of a **HOH** block in lobanovite; (*b*) oxygen atoms of the **O** layer: O(1) (pink) – apical vertex in DO_5 pyramid, O(2) (beige) and O(6) (grey) are apical vertexes in $T(2)O_4$ and $T(1)O_4$, respectively, and O(8) (red) corresponds to the OH group (H is white); (*c*) local environment of O(1), the apical anion in the DO_5 pyramid.

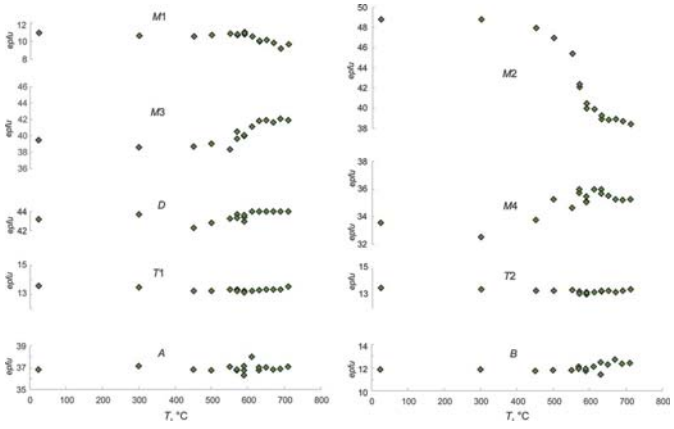

Figure 9
Variation in site scattering values with annealing temperature for lobanovite and its HT modification. Standard uncertainties are mainly within symbols. Note: small deviations in occupancies are attributed to atom disorder (the presence of low-intensity reflections in difference Fourier maps that cannot be included in the refinement).

Table 3
Bond valences in the crystal structure of lobanovite (Lb25) and its HT modification (Lb710).

Bond-valence parameters were taken from Gagné & Hawthorne (2015) calculated for site occupancies given in Table 2.

	M(1)	*M*(2)	*M*(3)	*M*(4)	*D*	*T*(1)	*T*(2)	*A*	*B*	O(1)	O(2)	O(3)	O(4)	O(5)	O(6)	O(7)	OH(8)	F
Lb25	1.17	1.92	2.06	2.07	4.03	3.93	3.93	0.80	1.25	2.06	1.92	1.97	1.95	2.02	1.98	1.97	1.05	0.14
Lb710	1.16	2.10	2.55	2.32	4.00	4.00	3.99	0.86	1.32	1.85	1.98	2.04	2.03	2.09	1.89	2.05	1.50	0.15

migration of Mg occurs from the *M*(3) and *M*(4) sites to the *M*(2) site (based on site scattering data and mean bond lengths). Below we also show evidence based on changes of interatomic distances that migration is more complex and involves (Mg+Mn) and Fe.

The loss of 6.7 electrons per formula unit (e.p.f.u) (∼2.7% of the total amount) in the total refined site scattering value for Lb710 compared with Lb25 (Table 2) can be explained by significant cation disorder as confirmed by some diffuse electron density in the difference Fourier maps. This seems to be common for annealed modifications since a similar loss of 2.2% of e.p.f.u. was observed in the recent study of riebeckite (Oberti *et al.*, 2018). Regarding this, the loss of site scattering at the *M*(1) site occupied by Na (Table 1) may refer either to real loss of some Na or originate from Na disorder. In either case, since the change in site scattering of *M*(1) is quite small, this effect is not decisive in the HT behaviour of lobanovite.

The defluorination of lobanovite on heating has not been detected in contrast to astrophyllite (Zhitova, Krivovichev *et al.*, 2017). According to our refinement the F atoms per formula unit (a.p.f.u) ranges from 0.12 to 0.22 in different grains with no correlation to annealing temperature. The absence of defluorination could be due to the minor Nb at the *D* site.

Inspection of Table 3 shows that some of the incident bond-valence sums deviate significantly from the values expected from the valence-sum rule, in particular the sums at *M*(2) and OH. The sum at *M*(2) is 2.10 valence units (v.u.) (Table 3) whereas the valence-sum rule and the assigned site populations suggest a value of 2.40 v.u. Similarly, the sum at OH(8) is 1.50 v.u. (Table 3) whereas the valence-sum rule and the assigned site populations suggest a value of 1.83 v.u. Similar behaviour was observed recently in heated dehydroxylated riebeckite (Oberti *et al.*, 2018). Here, the site population of the O(3) site is 1.90 O^{2-} + 0.10 F^{-}, and the incident bond valence at the O(3) site is 1.23 v.u. rather than the 1.90 v.u. required by the valence-sum rule. These anomalously low incident bond-valence sums are not unexpected. The oxidized dehydroxylated phases cannot be considered as stable phases in the long term. If they were, one would expect to find these oxidized dehydroxylated phases in the geological environment under suitable conditions. However, they are not found as stable phases in rocks of appropriate conditions of equilibration. These are highly strained structures that form as an intermediate product of a breakdown reaction, and significant deviations from the valence-sum rule are to be expected.

4.3. Mössbauer spectroscopy: derivation of site populations in lobanovite

The presence of two quadrupole-split doublets of equal intensity provides very important information about the site populations of Fe^{2+} in lobanovite: the Fe^{2+} ions belong to two groups with equal abundances, each group giving rise to one of the quadrupole-split doublets in the Mössbauer spectrum.

In order for the Fe^{2+} ions to belong to the two groups with equal abundances, either: (i) the various octahedra belong to two groups for which the next-nearest-neighbour arrangements are significantly different, thereby differently affecting the quadrupole splitting of Fe^{2+} in the two different arrangements; or (ii) the Fe^{2+} site populations of the three octahedra are such that the amount of Fe^{2+} in one octahedron is equal to the amount of Fe^{2+} in the other two octahedra.

First let us examine the next-nearest-neighbour arrangements of octahedra for each of the *M*(2), *M*(3) and *M*(4) octahedra:

M(2): $M(1)_2\ M(2)\ M(3)_2\ M(4)$
M(3): $M(1)\ M(2)_2\ M(4)_3$
M(4): $M(2)\ M(3)_3\ M(4)_2$

Each octahedron is surrounded by six other octahedra, but *M*(2) and *M*(3) are adjacent to *M*(1) which is occupied by Na, whereas *M*(4) is not adjacent to *M*(1). Thus Fe^{2+} may occupy two groups of sites with significantly different next-nearest-neighbour arrangements: [*M*(2) + *M*(3)] and *M*(4). The total refined site scattering (Hawthorne *et al.*, 1995) for these two groups of sites is as follows: [*M*(2) + *M*(3)] 88.4 e.p.f.u.; *M*(4) 33.5 e.p.f.u. In order for these two groups to contain equal amounts of Fe^{2+}, the amount of Fe^{2+} cannot exceed 2 × 33.5 = 67 e.p.f.u. = 2.60 Fe^{2+}. Lobanovite contains 3.24 a.p.f.u. Fe^{2+} and hence variation in the next-nearest-neighbour arrangements about the *M* octahedra cannot account for the presence of two quadrupole-split doublets of equal intensity in the Mössbauer spectrum of lobanovite.

Next let us examine the possibility that the amount of Fe^{2+} in one octahedron is equal to the amount of Fe^{2+} in the other two octahedra. The site populations of the *M*(2), *M*(3) and *M*(4) octahedra may be written as follows: $M(2) = Fe_xM_{(2-x)}$; $M(3) = Fe_yM_{(2-y)}$; $M(4) = Fe_zM_{(2-z)}$.

In order for any combination of two octahedra to contain the same amount of Fe^{2+} as the third octahedra, $x + y = z$ or $y + z = x$ or $z + x = y$. As the *M*(2) site has the highest refined site scattering, only the equation $y + z = x$ gives a feasible solution. There is an additional equation that relates *x*, *y* and *z* to the total amount of Fe^{2+} in the mineral: $x + y + z = 3.24$ (a.p.f.u. Fe^{2+}). The requirement that the amount of Fe^{2+} in the *M*(2)

site is equal to that in the $M(3) + M(4)$ sites gives $x = 3.24/2 = 1.62$ Fe^{2+} per formula unit. The remaining cations to be assigned to the $M(2)$, $M(3)$ and $M(4)$ sites are: Mn 0.45; Mg 2.30. Thus we may write the following equations relating the site populations to the refined site scattering values:

$M(2)$: $Fe^{2+}_{1.62}M_{0.38}$ = 48.9 e.p.f.u.

$M(3)$: $Fe^{2+}_{y}M_{(2-y)}$ = 39.5 e.p.f.u.

$M(4)$: $Fe^{2+}_{z}M_{(2-z)}$ = 33.5 e.p.f.u.

The equation for the $M(2)$ site may be solved directly: $M(2) = Fe^{2+}_{1.62}Mg_{0.21}Mn_{0.17}$ = 48.9 e.p.f.u., which indicates the close agreement between the refined and calculated site scattering. This leaves 1.62 Fe + 0.28 Mn + 2.09 Mg to be assigned to the $M(3)$ and $M(4)$ sites. There is no way to uniquely assign three cations to two sites given only the refined site scattering values (Hawthorne, 1983), and we must combine Fe ($Z = 26$) and Mn ($Z = 25$), Fe = 1.90, Mg = 2.09 a.p.f.u., to assign to the $M(3)$ and $M(4)$ sites.

$M(3)$: $y \times 26 + (2-y) \times 12 = 39.5$ e.p.f.u.

$M(4)$: $z \times 26 + (2-z) \times 12 = 33.5$ e.p.f.u.

Solving these two equations gives the following result: $y = 1.11$, $z = 0.68$. Thus we have the following site populations:

$M(1)$ = Na

$M(2)$ = 1.62 Fe^{2+} + 0.21 Mg + 0.17 Mn = 48.9 e.p.f.u.

$M(3)$ = 1.11 (Fe^{2+} + Mn) + 0.89 Mg = 39.5 e.p.f.u.

$M(4)$ = 0.68 (Fe^{2+} + Mn) + 1.32 Mg = 33.5 e.p.f.u.

where $^{M(3)}Fe^{2+} + {}^{M(4)}Fe^{2+}$ = 1.62 a.p.f.u.

4.4. Redistribution of cations in lobanovite on heating by Mössbauer spectroscopy and changes in bond distances (single-crystal X-ray diffraction)

As indicated by the Mössbauer spectra (Fig. 3), there is virtually no oxidation of Fe^{2+} at 450°C, ~15% oxidation at 550°C, and the absence of the peak at ~2.5 mm s^{-1} at 630°C indicates that the oxidation is complete by this temperature. The two Fe^{2+} quadrupole-split doublets of equal intensity persist at least until 550°C, strongly suggesting that oxidation of Fe^{2+} occurs randomly at the $M(1)$, $M(2)$ and $M(3)$ sites up to this temperature. With the increasing temperature, one can see the appearance and gradual growth of three sets of quadrupole-split doublets below 2 mm s^{-1}, and the corresponding isomer shifts indicate that these doublets are due to Fe^{3+}. Four of the six component lines are positionally distinct

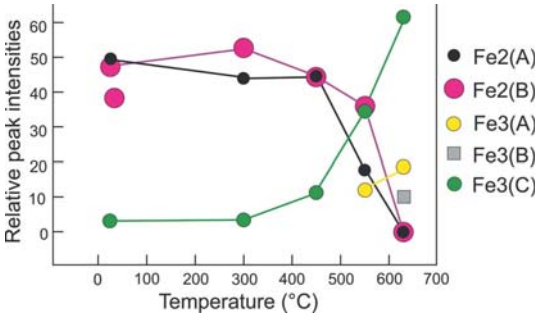

Figure 10
The variation in intensity of the Mössbauer peaks as a function of annealing temperature.

Table 4
Mössbauer parameters for lobanovite treated at different temperatures.

Fe2 and Fe3 correspond to Fe^{2+} and Fe^{3+}. QS is quadrupole splitting, IS is isomer shift and Fe(3)(?) is the peak assigned to Fe^{3+} when the site cannot be determined reliably.

	Site	QS (mm s^{-1})	IS (mm s^{-1})	FWHM	Relative intensity (%)
Lb25	Fe2(A)	2.929	0.896	0.286	49.6
	Fe2(B)	2.435	0.899	0.291	47.3
	Fe3(C)	1.159	0.225	0.548	3.1
Lb300	Fe2(A)	2.939	0.898	0.270	44.0
	Fe2(B)	2.448	0.899	0.313	52.6
	Fe3(C)	1.153	0.248	0.620	3.4
Lb450	Fe2(A)	2.928	0.895	0.291	44.5
	Fe2(B)	2.430	0.900	0.302	44.3
	Fe3(C)	1.328	0.258	0.693	11.2
Lb550	Fe2(A)	2.953	0.874	0.257	17.7
	Fe2(B)	2.399	0.902	0.412	35.9
	Fe3(A)	2.486	0.129	0.436	11.9
	Fe3(C)	1.260	0.208	0.600	34.5
Lb630	Fe3(A)	2.620	0.112	0.331	18.5
	Fe3(B)	2.355	0.135	0.285	10.0
	Fe3(C)	1.324	0.171	0.535	61.5
	Fe3(?)	0.713	0.123	0.277	10.0

from the Fe^{2+} doublets, and two of the lower-velocity Fe^{3+} peaks overlap with the lower-velocity Fe^{2+} peaks until the latter disappear at (or before) 630°C.

Fig. 10 shows the variation in intensity of the Mössbauer peaks as a function of annealing temperature, and the Mössbauer parameters are listed in Table 4. It is apparent from the values of the isomer shift for each of the bands that bands having isomer shift values in the range 0.12–0.35 mm s^{-1} (labelled Fe3) arise from octahedrally coordinated Fe^{3+}, whereas bands having isomer shift values in the range 0.87–0.90 mm s^{-1} (labelled Fe2) arise from octahedrally coordinated Fe^{2+}. As discussed above for the Mössbauer spectrum of Lb25, the two Fe^{2+} doublets arise from Fe^{2+} at $M(2)$ and $M(3)$+$M(4)$. It is apparent from Fig. 10 that Fe^{2+} at $M(2)$ and $M(3)$+$M(4)$ is oxidized to Fe^{3+} more or less at the same rate with the increasing treatment temperature. Below 500°C, there is only one single doublet due to Fe^{3+}: Fe3(C); obviously, Fe^{2+} is oxidizing at both $M(2)$ and $M(3)$+$M(4)$ and Fe^{3+} must occur at more than one crystallographic site, presumably $M(2)$, $M(3)$ and $M(4)$. However, additional processes are going on in this temperature range. As shown in Fig. 9, there is a strong decrease in the site scattering at the $M(2)$ site beginning at ~400°C and a concomitant increase in the site scattering at the $M(4)$ site. Just above 500°C, the scattering at the $M(3)$ site starts to increase (Fig. 9), there is a marked further decrease in the scattering at the $M(2)$ site (Fig. 9), and at 550°C additional Fe^{3+} doublets Fe3(A) and Fe3(B) appear and increase in intensity with the further increase in annealing temperature.

4.5. Changes in bond distances by single-crystal X-ray diffraction: evidence of Mn migration

Inspection of Table 2 shows that cation exchange in this temperature range is restricted to the $M(2)$, $M(3)$ and $M(4)$

sites. As noted above, Fe must migrate from $M(2)$ to $M(3)$ and $M(4)$, exchanging with Mg, which accounts for the changes in scattering values and the differences in bond lengths between Lb25 and Lb710 (Table 2). Although the increase in site scattering at the $M(3)$ and $M(4)$ sites is equal over the temperature range 25–710°C, $\langle M(3)\text{–O}\rangle$ decreases by 0.050 Å, almost three times as much as $\langle M(4)\text{–O}\rangle$ at −0.014 Å. In addition, $M(2)$ shows the largest change in site scattering between 25 and 710°C, −10 electrons (Table 2), while showing a small change in the mean bond length: −0.033 Å. If the cation exchange involves just Fe^{3+} and Mg, these differences in behaviour are not possible: another cation must be involved. The only other constituent that can be involved in this exchange is Mn. As we have shown above, there is 0.17 Mn^{2+} at the $M(2)$ site and 0.28 Mn^{2+} at the $M(3)$+$M(4)$ sites. The relative change in the mean bond lengths for the $M(3)$ and $M(4)$ sites indicates that there is an exchange of Mn^{2+} for Fe^{3+} from $M(3)$+$M(4)$ to $M(2)$.

5. Discussion

5.1. The role of Ti coordination in HT behaviour: comparison of lobanovite with five-coordinated Ti to astrophyllite with six-coordinated Ti

The geometrical changes for lobanovite at HT (Section 4) are very similar to those previously described for astrophyllite (Zhitova, Krivovichev *et al.*, 2017). However, the redistribution of Fe and Mg+Mn cations in the **O** layer in lobanovite is unique, at least for titanosilicates as discussed in detail below.

In astrophyllite, the $D\varphi_6$ (D = Ti, φ = O, OH, F) octahedron is distorted because of the Jahn–Teller effect (Kunz & Brown, 1995) via displacement of Ti from the geometrical centre and formation of one short ~1.81 Å and one long ~2.10 Å apical Ti–φ bond (Fig. 11). In the HT modification of astrophyllite, Ti shifts to the centre of the octahedron, forming a near-regular $D\varphi_6$ octahedron with similar apical Ti–φ bonds: 1.95 and 1.98 Å (Fig. 11), respectively (Zhitova, Krivovichev *et al.*, 2017). The shift of Ti by ~0.15 Å along the apical axis of the $D\varphi_6$ octahedron is caused by the additional bond valence incident at the O(2) atom from **O**-layer cations, when oxidation of Fe occurs at the $M(1)$–$M(4)$ sites. In this case, the shift of Ti observed in the HT modification of astrophyllite (Fig. 11) stabilizes the structure as elongation of the Ti–O(2) bond compensates for the excess bond valence contributed by oxidized cations of the **O** layer.

However, such a mechanism of structural stabilization is not possible for lobanovite as the D site is mainly five-coordinated, *i.e.* is the centre of the DO_5 square pyramid with the Ti position almost fixed. It is noteworthy that the amount of bond valence contributed by cations of the **O** layer to the O(1) apical oxygen of the DO_5 pyramid is of crucial crystal-chemical significance as it determines the position of Ti along the apical axis [Fig. 11(*c*)], and therefore the Ti coordination (Fig. 11) (McDonald *et al.*, 2000; Sokolova, 2006). In the structure of lobanovite, the O(1) atom receives ~0.8 v.u. from three M sites (M^+ and $2M^{2+}$) in the **O** layer (in astrophyllite, this value is ~1 v.u. from three M^{2+} sites), and hence the apical Ti–O(1) bond in lobanovite is short, ~1.75 Å (in astrophyllite, this bond is ~1.85 Å long), and Ti is five-coordinated in lobanovite [Fig. 11(*c*)]. Hypothetically, there could be a bond-valence excess at the apical O(1) anion of the DO_5 pyramid as a result of the HT oxidation–dehydroxylation. However, this does not happen due to redistribution of Fe and Mg+Mn over the $M(2)$, $M(3)$, $M(4)$ sites accompanying iron oxidation and dehydroxylation. The O(1) atom is bonded to the cations at the $M(1)$ and two $M(2)$ sites [Fig. 8(*c*)] [in lobanovite $M(1)$ = Na; $M(2)$ = $Fe^{2+}_{1.62}Mg_{0.21}Mn_{0.17}$] and the Fe ↔ Mg+Mn exchange [seen in the HT modification: $M(1)$ = Na; $M(2)$ = $Fe^{3+}_{0.80}Mg_{0.75}Mn_{0.45}$] maintains the amount of bond valences received by O(1) (Table 3) and serves as a stabilization mechanism alternative to that observed in astrophyllite (with six-coordinated Ti).

To conclude, the redistribution of Fe and Mg+Mn over the $M(2)$, $M(3)$ and $M(4)$ sites is driven by iron oxidation coupled

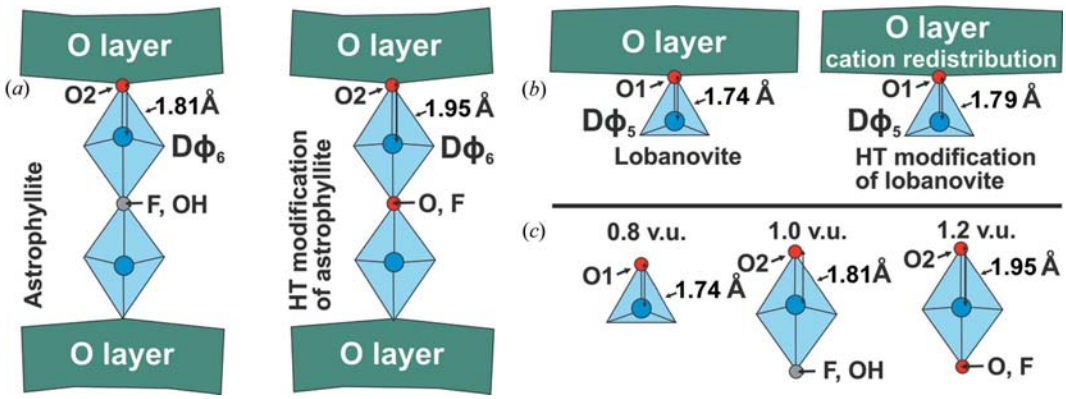

Figure 11
Schematic representation of changes in geometry of Ti polyhedra associated with thermally induced iron oxidation in (*a*) astrophyllite: Tiφ_6 octahedra become more regular due to iron oxidation (Zhitova, Krivovichev *et al.*, 2017); and (*b*) lobanovite: the geometry of the TiO_5 square pyramid is almost unchanged, the amount of incident bond valence at O(1) is maintained due to Fe^{3+}↔Mg+Mn migration over the $M(2)$, $M(3)$ and $M(4)$ sites (see details in the text). (*c*) The influence of incident bond valence at the apical oxygen of the Ti polyhedra on the geometry of Ti polyhedra.

with dehydroxylation, and produces an additional cation bond valence in the HT modification. Moreover, the pyramidal coordination of Ti cannot sustain the increased bond valence resulting from the iron oxidation. This instability can be accommodated by the substitution of Fe^{3+} at the $M(2)$ site [bonded to O(1) (Fig. 8)] by Mg+Mn. Rearrangement of Fe^{3+} ↔ Mg+Mn over the $M(2)$, $M(3)$, $M(4)$ sites produces a new bond-valence arrangement in the HT modification (Table 3) which increases the stability of the mineral on heating.

5.2. Brief comparison with micas, amphiboles and tourmalines

HT Fe^{2+}↔Mg exchange over two octahedrally coordinated sites has been widely studied for such rock-forming minerals as orthopyroxene (Kirfel, 1996; Wang *et al.*, 2005) and olivine (*e.g.* Henderson *et al.*, 1996; Rinaldi *et al.*, 2000; Heinemann *et al.*, 2006; Shi *et al.*, 2009; Taran & Matsyuk, 2013). Careful attention was paid to the kinetics of the process (by *in situ* HT experiments and quenching) and ordering and disordering of Fe^{2+} and Mg cations due to the importance of orthopyroxene and olivine as geothermometers (Ganguly *et al.*, 1994; Stimpfl *et al.*, 2005) and for the simulation of physical properties of the upper mantle (Akamatsu & Kumazawa, 1993). However, the Fe^{2+}↔Mg cation exchange in orthopyroxene and olivine at elevated temperatures does not involve iron oxidation or dehydroxylation, and the crystal-chemical reasons for this exchange are likely to be different from those suggested here for lobanovite.

HT iron oxidation–dehydroxylation coupled with Fe↔Mg exchange was observed for tourmalines: in oxy-dravite (Bosi *et al.*, 2016), where Fe–Mg redistribution over the Y and Z sites had been found (according to $^{Y}Fe + {}^{Z}Mg \rightarrow {}^{Z}Fe + {}^{Y}Mg$), while Al is almost unchanged; and in lucchesiite (Bosi *et al.*, 2017), where Fe–Mg–Al redistribution over the Y and Z sites occurs with the increase of Fe content in the Z site balanced by the increase of Mg and Al in the Y site. The Fe↔Al exchange was reported for fluor-elbaite via the reaction $^{Y}Fe + {}^{Z}(Mg + Al) \rightarrow {}^{Z}Fe + {}^{Y}(Mg + Al)$ (Bosi *et al.*, 2018). For these minerals, Fe order–disorder is strongly influenced by temperature rather than redox conditions. The study is important in terms of the use of tourmaline as a geothermometer.

The HT iron oxidation–dehydroxylation was widely described for amphiboles (Clowe *et al.*, 1988; Phillips *et al.*, 1988, 1989; Welch *et al.*, 2007, 2011; Zema *et al.*, 2012; Della Ventura *et al.*, 2017). For some of them, the ordering of cations at HT was described, which was interpreted as an attempt to re-equilibrate crystal structure at the experimental temperature (Zema *et al.*, 2012; Welch *et al.*, 2008). For instance, in riebeckite, both iron oxidation–dehydroxylation and migration of Fe from $M(2)$/$M(3)$ to $M(4)$ were registered, and the latter was interpreted as an attempt to complete deprotonation. The migration and oxidation of Fe produced a new cation distribution scheme for amphiboles that resulted in the novel charge distribution pattern with the increased stability of riebeckite phase to HT (Oberti *et al.*, 2018). In the case of another amphibole, gedrite, it was unclear whether cation ordering is driven by iron oxidation–dehydroxylation or is just a result of a HT treatment (Zema *et al.*, 2012).

Micas (phyllosilicates) are another group for which iron oxidation–dehydroxylation is widely registered at elevated temperatures, for example: Fe-rich phlogopite (Russell & Guggenheim, 1999; Chon *et al.*, 2006; Ventruti *et al.*, 2008; Zema *et al.*, 2010), illite (Murad & Wagner, 1996), biotite (Güttler *et al.*, 1989) and vermiculite (Veith, 1974). However, the cation migration in octahedral sheets was scarcely described either due to the experimental difficulties or its rarity. Nevertheless, the interchangeable migration of octahedral Fe and Mg cations accompanying iron oxidation–dehydroxylation was reported for dioctahedral micas: glauconites and celadonites (Tsipursky *et al.*, 1985; Muller *et al.*, 2000) at $T \geq 650$°C based on data obtained by transmission electron microscopy performed with the selected-area electron diffraction technique. The same method allowed for an identification of the new superstructure in annealed celadonite (Kogure *et al.*, 2007). In the HT dehydroxylated modifications of glauconites and celadonites, the ordering of Mg and Fe cations was observed with the formation of a configuration in which each M^{3+} cation is surrounded by three M^{2+} cations and *vice versa* (Muller *et al.*, 2000).

To conclude, the literature review shows that the HT behaviour of heterophyllosilicates has similar features to that of tourmalines, amphiboles and micas, not only in terms of iron oxidation–dehydroxylation but also in migration (diffusion) of Fe in the crystal structure of their HT modifications. From the papers cited above, we can assume that the driving force of Fe migration may be due to: (i) an attempt to complete iron oxidation, *i.e.* migration of Fe to a hydroxylated oxygen site (that is not the case for lobanovite since all M sites have equivalently hydroxylated environments) or (ii) the formation of a new charge (and bond strengths) distribution pattern sustainable for incorporation of ferric iron instead of initial ferrous iron. The latter is realized by a local re-ordering of atoms that also seems to be an issue for lobanovite; such modifications with rearranged atoms can be viewed as more stable ones, at least with respect to temperature as experiments on minerals show.

6. Conclusions and outlook

The present work reports for the first time the HT iron oxidation–dehydroxylation observed for lobanovite on heating (at $T > 450$°C) that occurs by the reaction $Fe^{2+} + OH^{-} \rightarrow Fe^{3+} + O^{2-} + \frac{1}{2}H_2\uparrow$ [from $K_2Na(Fe^{2+}{}_4Mg_2Na)Ti_2(Si_4O_{12})_2O_2(OH)_4$ to $K_2Na(Fe^{3+}{}_4Mg_2Na)Ti_2(Si_4O_{12})_2O_2O_4$] followed by the Fe ↔ Mg+Mn redistribution over the octahedral $M(2)$, $M(3)$ and $M(4)$ sites [Fe from $M(2)$ to $M(3)$ and $M(4)$ and the reverse for Mg+Mn]. The iron oxidation–dehydroxylation is outlined by the unit-cell contraction (X-ray diffraction data) mainly due to shortening of intermediate distance between adjacent **HOH** blocks; the evolution of Mössbauer spectra confirms the change of Fe oxidation state, while dehydroxylation is evident from the IR data. The Fe ↔ Mg+Mn interchangeable migration in the **O** layer is confirmed

by the site occupancies and bond lengths determined by means of single-crystal X-ray diffraction and Mössbauer spectroscopy on a set of quenched modifications. Despite the chemical and structural differences between lobanovite and its HT modification (Fe oxidation state and distribution of Fe and Mg+Mn cations in the octahedral layer), the HT modification is isotypic to parent lobanovite (monoclinic, *C*2/*m*), except for the loss of hydrogen. The driving force of the Fe ↔ Mg+Mn redistribution is to preserve bond strengths incident at the apical O atoms in the TiO_5 pyramids (*i.e.* to incorporate the excess bond strengths resulting from the iron oxidation–dehydroxylation without structure collapse). This is strikingly different from astrophyllite with six-coordinated Ti, where identical iron oxidation–dehydroxylation was accompanied by the changes of geometry of TiO_6 octahedra, which are more flexible in terms of geometry than TiO_5 square pyramids.

In general, the results show crystal-chemical similarities in the HT behaviour of heterophyllosilicates, micas, tourmalines and amphiboles containing both Fe^{2+} and hydroxyl ions, since all of them undergo iron oxidation–dehydroxylation that, in some cases, is coupled with the redistribution of octahedral Fe and Mg cations. The results obtained in this work for lobanovite and its HT modification shed some light on general mechanisms of HT behaviour for the mineral groups mentioned above, owing to the fact that lobanovite is a well-characterized mineral with stable chemical composition, a good quality of crystals (that maintain crystallinity upon annealing), the high content of Fe^{2+} and OH groups in octahedral layers and available in relatively large quantities that enable multi-methodological studies to be conducted. In addition, it seemed striking to us that lobanovite undergoes the Fe ↔ Mg+Mn rearrangement within an hour of annealing (see Section 2).

The potential application of the results may be in the production of materials with desirable properties. As we note in Section 1, the layered topology of lobanovite is similar to that of other minerals and materials with widely applied **TOT** structures. The results on HT transformation of lobanovite point to more complex and flexible crystal chemistry of the mineral and the possibility of variation in the distribution of bond valences within one isotypic structure potentially affecting its properties. Here we have also shown that the quenched 'oxy' forms of lobanovite are possible, in a crystal-chemical sense, and therefore may potentially occur in nature although under very peculiar conditions. One possible way in which they may occur is during post-crystallization short-term heating.

Acknowledgements

We thank Natalia Vlasenko for collection of the scanning electron microscopy data. The study was carried out at the X-ray diffraction and Geomodel Resource Centres of St Petersburg State University. We are grateful to Fernando Cámara and an anonymous reviewer for their suggestions.

Funding information

The following funding is acknowledged: Russian Science Foundation (grant No. 17-77-10023 to Elena Zhitova).

References

Agakhanov, A. A., Pautov, L. A., Sokolova, E., Abdu, Ya. A. & Karpenko, V. Y. (2016). *Can. Mineral.* **54**, 33–48.
Akamatsu, T. & Kumazawa, M. (1993). *Phys. Chem. Miner.* **19**, 423–430.
Belousov, R. & Filatov, S. (2007). *Glass Phys. Chem.* **33**, 271–275.
Bosi, F., Skogby, H. & Hålenius, U. (2016). *Contrib. Mineral. Petrol.* **171**, 47.
Bosi, F., Skogby, H. & Hålenius, U. (2018). *Phys. Chem. Miner.* **45**, 371–383.
Bosi, F., Skogby, H., Hålenius, U. & Ciriotti, M. E. (2017). *Phys. Chem. Miner.* **45**, 621–632.
Bruker (2009). *Topas V4.2: General Profile and Structure Analysis Software for Powder Diffraction Data*. Bruker AXS, Karlsruhe, Germany.
Bruker (2014). *APEX2*. Version 2014.11-0. Bruker AXS, Madison, Wisconsin, USA.
Bubnova, R. S., Firsova, V. A. & Filatov, S. K. (2013). *Glass Phys. Chem.* **39**, 347–350.
Cámara, F., Sokolova, E., Abdu, Y. & Hawthorne, F. C. (2010). *Can. Mineral.* **48**, 1–16.
Chon, C.-M., Lee, C.-K., Song, Y. & Kim, S. A. (2006). *Phys. Chem. Miner.* **33**, 289–299.
Clowe, C. A., Popp, R. K. & Fritz, S. J. (1988). *Am. Mineral.* **73**, 487–499.
Ferraris, G. (2005). *Rev. Mineral. Geochem.* **57**, 69–104.
Ferraris, G. (2008). *Z. Kristallogr.* **223**, 76–84.
Ferraris, G., Bloise, A. & Cadoni, M. (2008). *Microporous Mesoporous Mater.* **107**, 108–112.
Gagné, O. C. & Hawthorne, F. C. (2015). *Acta Cryst.* B**71**, 562–578.
Ganguly, J., Yang, H. & Ghose, S. (1994). *Geochim. Cosmochim. Acta*, **58**, 2711–2723.
Güttler, B., Niemann, W. & Redfern, S. A. T. (1989). *Mineral. Mag.* **53**, 591–602.
Hawthorne, F. C. (1983). *Am. Mineral.* **68**, 287–306.
Hawthorne, F. C., Ungaretti, L. & Oberti, R. (1995). *Can. Mineral.* **33**, 907–911.
Heinemann, R., Kroll, H., Kirfel, A. & Barbier, B. (2006). *Eur. J. Mineral.* **18**, 673–689.
Henderson, C. M. B., Knight, K. S., Redfern, S. A. T. & Wood, B. J. (1996). *Science*, **271**, 1713–1715.
Jin, S., Xu, H., Lee, S. & Fu, P. (2018). *Acta Cryst.* B**74**, 1–11.
Kirfel, A. (1996). *Phys. Chem. Miner.* **23**, 503–519.
Kogure, T., Kameda, J. & Drits, V. A. (2007). *Am. Mineral.* **92**, 1531–1534.
Kunz, M. & Brown, I. D. (1995). *J. Solid State Chem.* **115**, 395–406.
Langreiter, T. & Kahlenberg, V. (2015). *Crystals*, **5**, 143–153.
Lykova, I. S., Chukanov, N. V., Kazakov, A. I., Tarasov, V. P., Pekov, I. V., Yapaskurt, V. O. & Chervonnaya, N. A. (2013). *Phys. Chem. Miner.* **40**, 625–633.
Lykova, I. S., Chukanov, N. V., Tarasov, V. P., Pekov, I. V. & Yapaskurt, V. O. (2013). *Russ. J. Phys. Chem. B Focus Phys.* **32**, 35–42.
Lykova, I. S., Pekov, I. V., Zubkova, N. V., Chukanov, N. V., Yapaskurt, V. O., Chervonnaya, N. A. & Zolotarev, A. A. (2015*a*). *Eur. J. Mineral.* **27**, 535–549.
Lykova, I. S., Pekov, I. V., Zubkova, N. V., Yapaskurt, V. O., Chervonnaya, N. A., Zolotarev, A. A. & Giester, G. (2015*b*). *Eur. J. Mineral.* **27**, 669–682.
McDonald, A. M., Grice, J. D. & Chao, G. Y. (2000). *Can. Mineral.* **38**, 649–656.
Momma, K. & Izumi, F. (2011). *J. Appl. Cryst.* **44**, 1272–1276.

Mukherjee, S. (2013). *The Science of Clays*. Netherlands: Springer Science and Business Media.
Muller, F., Drits, V. A., Tsipursky, S. I. & Plançon, A. (2000). *Clay Miner.* **35**, 505–514.
Murad, E. & Wagner, U. (1996). *Clay Miner.* **31**, 45–52.
Murray, H. H. (1991). *Appl. Clay Sci.* **5**, 379–395.
Oberti, R., Boiocchi, M., Zema, M., Hawthorne, F. C., Redhammer, G. J., Susta, U. & Ventura, G. D. (2018). *Eur. J. Mineral.* **30**, 437–449.
Peng, S. & Ma, Z. (1963). *Sci. Sin.* **12**, 272–276.
Phillips, M. W., Draheim, J. E., Popp, R. K., Clowe, C. A. & Pinkerton, A. A. (1989). *Am. Mineral.* **74**, 764–773.
Phillips, M. W., Popp, R. K. & Clowe, C. A. (1988). *Am. Mineral.* **73**, 500–506.
Piilonen, P. C., Lalonde, A. E., McDonald, A. M., Gault, R. A. & Larsen, A. O. (2003). *Can. Mineral.* **41**, 1–26.
Piilonen, P. C., McDonald, A. M. & Lalonde, A. E. (2003). *Can. Mineral.* **41**, 27–54.
Rinaldi, R., Artioli, G., Wilson, C. C. & McIntyre, G. (2000). *J. Phys. Chem.* **27**, 623–629.
Robinson, K., Gibbs, G. V. & Ribbe, P. H. (1971). *Science*, **172**, 567–570.
Russell, R. L. & Guggenheim, S. (1999). *Can. Mineral.* **37**, 711–729.
Shannon, R. D. (1976). *Acta Cryst.* A**32**, 751–767.
Sheldrick, G. M. (2015). *Acta Cryst.* A**71**, 3–8.
Shi, J., Ganschow, S., Klimm, D., Simon, K., Bertram, R. & Becker, K.-D. (2009). *J. Phys. Chem. C*, **113**, 6267–6274.
Shi, N., Ma, Z., Li, G., Yamnova, N. A. & Pushcharovsky, D. Y. (1998). *Acta Cryst.* B**54**, 109–114.
Sokolova, E. (2006). *Can. Mineral.* **44**, 1273–1330.
Sokolova, E. & Cámara, F. (2008). *Eur. J. Mineral.* **20**, 253–260.
Sokolova, E., Cámara, F., Hawthorne, F. C. & Ciriotti, M. E. (2017*a*). *Mineral. Mag.* **81**, 143–153.
Sokolova, E., Cámara, F., Hawthorne, F. C., Semenov, E. I. & Ciriotti, M. E. (2017*b*). *Miner. Mag.* **81**, 175–181.
Sokolova, E., Day, M. C., Hawthorne, F. C. & Kristiansen, R. (2018). *Mineral. Mag.* **82**, 243–255.
Sokolova, E. & Hawthorne, F. C. (2016). *Can. Mineral.* **54**, 1539–1547.
Stepanov, A. V., Bekenova, G. K., Levin, V. L., Sokolova, E., Hawthorne, F. C. & Dobrovol'skaya, E. A. (2012). *Can. Mineral.* **50**, 159–168.
Stimpfl, M., Ganguly, J. & Molin, G. (2005). *Contrib. Mineral. Petrol.* **150**, 319–334.
Taran, M. N. & Matsyuk, S. S. (2013). *Phys. Chem. Miner.* **40**, 309–318.
Tsipursky, S. I., Drits, V. A. & Plançon, A. (1985). *Sov. Phys. Crystallogr.* **30**, 38–44.
Veith, J. A. (1974). *Clays Clay Miner.* **22**, 345–353.
Ventruti, G., Zema, M., Scordari, F. & Pedrazzi, G. (2008). *Am. Mineral.* **93**, 632–643.
Ventura, G. D., Susta, U., Bellatreccia, F., Marcelli, A., Redhammer, G. & Oberti, R. (2017). *Am. Mineral.* **102**, 117–125.
Wang, L., Moon, N., Zhang, Y., Dunham, W. & Essene, E. (2005). *Geochim. Cosmochim. Acta*, **69**, 5777–5788.
Welch, M. D., Cámara, F. & Oberti, R. (2011). *Phys. Chem. Miner.* **38**, 321–334.
Welch, M. D., Cámara, F., Ventura, G. D. & Iezzi, G. (2007). *Rev. Mineral. Geochem.* **67**, 223–260.
Welch, M. D., Reece, J. J. & Redfern, S. A. T. (2008). *Mineral. Mag.* **72**, 877–886.
X-ray Laboratory, Hubei Geologic College (1974). *Sci. Sin.* **1**, 18–33.
Yakovenchuk, V., Ivanyuk, G., Pakhomovsky, Ya. & Men'shikov, Yu. (2005). *Khibiny*. Apatity: Laplandia Minerals.
Zema, M., Ventruti, G., Lacalamita, M. & Scordari, F. (2010). *Am. Mineral.* **95**, 1458–1466.
Zema, M., Welch, M. D. & Oberti, R. (2012). *Contrib. Mineral. Petrol.* **163**, 923–937.
Zhitova, E. S., Krivovichev, S. V., Hawthorne, F. C., Krzhizhanovskaya, M. G., Zolotarev, A. A., Abdu, Ya. A., Yakovenchuk, V. N., Pakhomovsky, Ya. A. & Goncharov, A. G. (2017). *Phys. Chem. Miner.* **44**, 595–613.
Zhitova, E. S., Panikorovskii, T. L., Yakovenchuk, V. N. & Krzhizhanovskaya, M. G. (2018). *Zap. RMO*, **147**, 82–94.
Zhitova, E. S., Zolotarev, A. A., Krivovichev, S. V., Goncharov, A. G., Gabdrakhmanova, F. A., Vladykin, N. V., Krzhizhanovskaya, M. G., Shilovskikh, V. V., Vlasenko, N. S. & Zolotarev, A. A. (2017). *Hyperfine Interactions*, **238**, 96.